Low-Dimensional Transport and Large Thermoelectric Power Factors in Bulk Semiconductors by Band Engineering of Highly Directional Electronic States

Daniel I. Bilc,[1,2] Geoffroy Hautier,[3] David Waroquiers,[3] Gian-Marco Rignanese,[3] and Philippe Ghosez[1]
[1]Theoretical Materials Physics, Université de Liège, 4000 Sart Tilman, Belgium
[2]Molecular and Biomolecular Physics Department, National Institute for Research and Development of Isotopic and Molecular Technologies, RO-400293 Cluj-Napoca, Romania
[3]Institute of Condensed Matter and Nanosciences, Université catholique de Louvain, 1348 Louvain-la-neuve, Belgium
(Received 4 September 2014; published 31 March 2015)

Thermoelectrics are promising for addressing energy issues but their exploitation is still hampered by low efficiencies. So far, much improvement has been achieved by reducing the thermal conductivity but less by maximizing the power factor. The latter imposes apparently conflicting requirements on the band structure: a narrow energy distribution and a low effective mass. Quantum confinement in nanostructures and the introduction of resonant states were suggested as possible solutions to this paradox, but with limited success. Here, we propose an original approach to fulfill both requirements in bulk semiconductors. It exploits the highly directional character of some orbitals to engineer the band structure and produce a type of low-dimensional transport similar to that targeted in nanostructures, while retaining isotropic properties. Using first-principle calculations, the theoretical concept is demonstrated in Fe_2YZ Heusler compounds, yielding power factors 4 to 5 times larger than in classical thermoelectrics at room temperature. Our findings are totally generic and rationalize the search of alternative compounds with similar behavior. Beyond thermoelectricity, these might be relevant also in the context of electronic, superconducting, or photovoltaic applications.

DOI: 10.1103/PhysRevLett.114.136601 PACS numbers: 72.20.Pa, 71.15.Mb, 71.20.Nr

Thermoelectricity, realizing the direct conversion between thermal and electrical energies, is a very promising avenue for renewable energy generation. The efficiency of a thermoelectric (TE) material can be described by its figure of merit ZT, defined as $ZT = (S^2\sigma T)/(\kappa_e + \kappa_l)$, where S is the thermopower, σ the electrical conductivity, T the absolute temperature, and κ_e and κ_l the electronic and lattice contributions to the thermal conductivity. In practice, ZT should be greater than 3 for TE devices to become fully competitive with other energy conversion systems [1,2]. Unfortunately, more than fifty years after the promising discovery of Bi_2Te_3-based alloys with $ZT \sim 1$ [3], increasing ZT further remains a real challenge. Huge efforts have been dedicated to the lowering of κ_l using specific crystal structures (e.g., phonon glass-electron crystals [4]) and nanostructuring [5–9], leading to the generation of materials with $ZT = 1$–2.4 within the last decade [10–12]. Record low values of $\kappa_l = 0.22 - 0.5$ W/mK [8,10] were achieved, and it is unlikely that these values can still be significantly decreased. At this stage, as emphasized by Kanatzidis [8], the next step forward should come from new breakthrough ideas on how to significantly enhance $S^2\sigma$, the power factor (PF).

A promising avenue was proposed by Hicks and Dresselhaus [5,13], who predicted theoretically that quantum confinement of electrons in multiple wells can substantially increase the PF. It was confirmed experimentally that the PF in the confined region of nanostructures [14,15] can indeed be larger than in related bulks. However, the gain in the confined region is partly counterbalanced by the contribution from the barrier material producing the confinement. More recently, Mahan and Sofo [16] searched for what should be the ideal shape of the so-called transport distribution function that optimizes ZT. They reached the conclusion that the best materials would combine (i) a distribution of carrier energy as narrow as possible and (ii) high carrier velocities in the direction of the applied field. Satisfying both of these criteria seems difficult in practice: narrow energy distributions are typically associated with flat energy bands, while high carrier velocities are necessarily associated with highly dispersive bands. This could be partly achieved in rare-earth compounds like $YbAl_3$, yielding very large PF at low temperatures [17]. However, those are metals with TE properties rapidly decreasing with increasing T. Alternatively, attempts to combine these apparently incompatible requirements in semiconductors have relied on the "band structure engineering" of narrow energy features in the density of states from in-gap and resonant states near the band edges [18–22].

Here, we show theoretically that the seemingly conflicting requirements formulated by Mahan and Sofo [16] can actually be combined within the same band of certain semiconductors, exploiting the highly directional character of some orbitals. This is achieved without any nanostructuring or introduction of resonant states. It yields, in the bulk phase, a type of low-dimensional transport similar to that targeted by Hicks and Dresselhaus in nanostructures [5], while simultaneously retaining isotropic transport properties

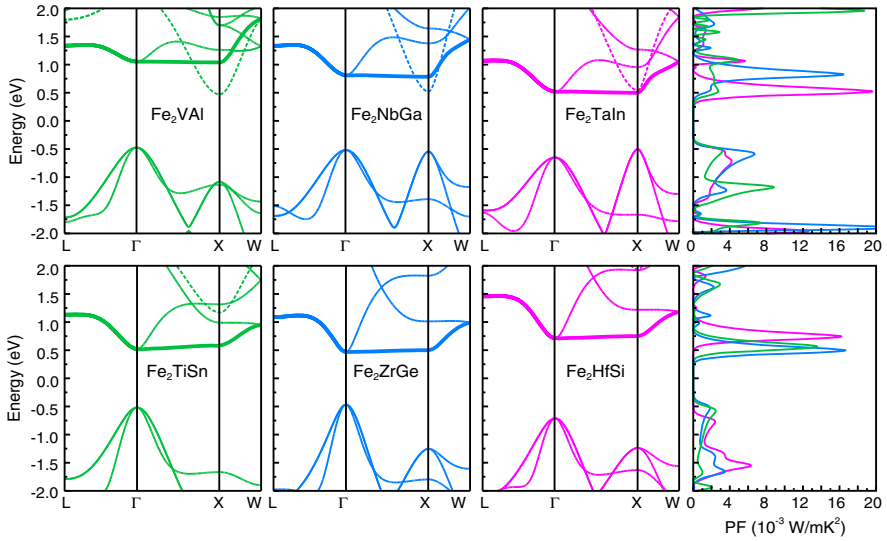

FIG. 1 (color online). Electronic band structures and power factors (PF $= S^2\sigma$) at 300 K for the sets S1 and S2 of compounds. Fe_2YZ full Heusler compounds with $Y =$ V (green lines), Nb (blue lines), Ta (magenta lines) and $Z =$ Al, Ga, In in the first row. Fe_2YZ full Heusler compounds with $Y =$ Ti (green lines), Zr (blue lines), Hf (magenta lines) and $Z =$ Sn, Ge, Si in the second row. Dotted lines indicate the highly dispersive lowest conduction band of dominant Y e_g character. The bold lines show the band of Fe e_g character that is flat along the ΓX direction and highly dispersive along others.

at the macroscopic level, concretizing ideas recently proposed by Parker *et al.* [23]. The concrete consequences of this finding on the TE properties is demonstrated in the class of Fe_2YZ full Heusler compounds: by engineering the appearance of Fe e_g states at the bottom of the conduction bands, power factors 4 to 5 times larger than in classical thermoelectrics (such as PbTe or Bi_2Te_3) can be obtained at room temperature. Beyond revealing the unexpected interest of a class of compounds often considered as modest thermoelectrics [24], our results rationalize the search of alternative compounds with an optimal power factor. The underlying concepts are totally generic and can be combined with other known strategies for decreasing the thermal conductivity in order to increase the TE figure of merit.

The electronic properties were studied within density functional theory using CRYSTAL [25]. We adopted a B1-WC hybrid functional scheme [26] which was previously shown to be accurate for describing the electronic and TE properties of this class of compounds [21]. The electronic transport properties were studied within the Boltzmann transport formalism and constant relaxation time approximation implemented in BoltzTraP [27]. Within this approximation, S is independent of the relaxation time τ, whereas σ and PF depend linearly on τ. The relaxation time was set to $\tau = 3.4 \times 10^{-14}$ s in all of the calculations. This value was determined by fitting the electrical resistivity ρ to the experimental value of 0.65 mΩ cm for $Fe_2VAl_{1-x}M_x$ ($M =$ Si, Ge) systems at doping $x = 0.03$ and 300 K [24,28]. For Fe_2VAl, the calculated PF is 3 mW/mK^2 (Fig. 1), in close agreement with experimental data. In order to estimate with more accuracy ZT at high T, we went beyond constant relaxation time approximation and considered T and energy E dependences of the relaxation time $\tau(T, E)$ for the acoustic and polar optical phonon scattering mechanisms (Ref. [29], text). The thermodynamical stability was assessed using the generalized gradient approximation from Perdew, Burke and Ernzheroff within a plane augmented wave approach and using VASP [53,54]. The computational parameters and pseudopotentials are similar to the ones used in the Materials Project [55,56]. For each chemical system (e.g., Fe-Ti-Sn), we computed the chemistry in the Heusler crystal structure but also other ternary crystal structures obtained from Heusler-forming systems. The stability of each Heusler phase was evaluated versus all phases present in the Materials Project and our generated ternary phases using the convex hull construction implemented in the PYMATGEN package [57].

We start our search from Fe_2VAl, which, in spite of relatively modest TE properties ($ZT \sim 0.13 - 0.2$ [24,58], PF $=$ 4–6 mW/mK^2 [24,28] at 300–400 K), is considered for low-cost TE applications [59]. As clarified recently [21], it is an intrinsic semiconductor, with a low band gap between the highest valence bands of dominant Fe t_{2g} character and a highly dispersive lowest conduction band of dominant V e_g character (see the dotted line in Fig. 1). Interestingly Fe_2VAl also exhibits a "flat-and-dispersive" band of Fe e_g character that is very flat along the ΓX direction of the Brillouin zone and highly dispersive along others (see the bold line in Fig. 1). This band combines the above-mentioned features identified by Mahan and Sofo to produce a large PF. It lies, however, $\sim$0.6 eV above the bottom of the conduction band and is not active in transport at room temperature for optimal doping at electron concentrations $n \sim 10^{19}$ cm^{-3}. In order to move its position towards the bottom of the conduction band, we performed atomic substitutions at the Y and Z sites.

We consider in Fig. 1 a first set (S1) of Fe_2YZ full Heusler compounds with $Y =$ V, Nb, Ta and $Z =$ Al, Ga, In. Going from 3d to 5d transition metal elements at the Y site tends to move the Y e_g dispersive band upwards. Furthermore, going to higher-mass elements at the Y and Z sites increases the lattice parameter (and the Fe-Fe distance), resulting in a decrease of Fe-Fe interactions lowering the Fe e_g levels (Ref. [29], text). Consequently, in many compounds, the Fe e_g flat-and-dispersive band appears close to the bottom of the conduction band. In line

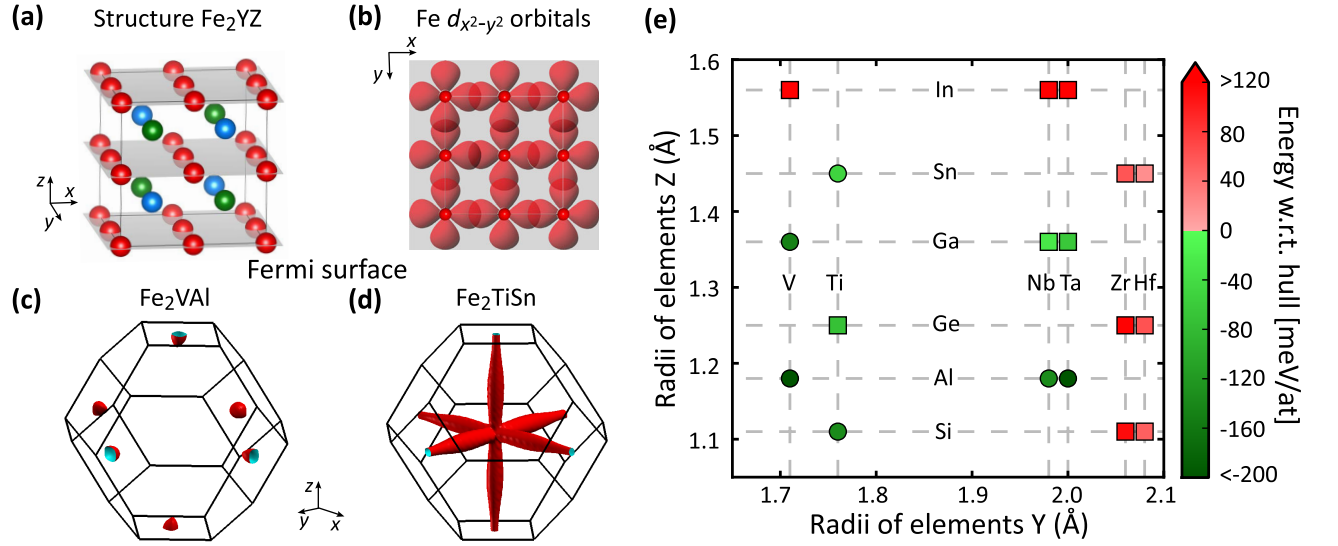

FIG. 2 (color online). Atomic structure, Fermi surfaces, and thermodynamical stability of Fe_2YZ compounds. (a) Full Heusler structure consisting of four interpenetrating fcc lattices with Fe, Y, and Z atoms represented in red, green and blue. It can also be viewed as alternating Fe_2 and YZ planes along the {001} (see Fe_2 planes highlighted in grey), {100}, and {010} directions. (b) Sketch of the Fe $d_{x^2-y^2}$ e_g orbitals overlapping in {001}-Fe_2 planes. (c,d) Fermi surfaces of Fe_2VAl and Fe_2TiSn at doping concentration yielding the maximum PFs at 300 K. (e) Map of the thermodynamical stability (as measured by the energy with respect to hull) computed at 0 K as a function of the Y and Z atomic radii. A negative number (inverse energy above hull, green color) corresponds to a stable phase and a positive number (energy above hull, red color) to an unstable one. Circles (resp. squares) correspond to compounds (resp. not) previously synthesized.

with our expectations, this increases the PFs at 300 K from ~3 mW/mK^2 for Fe_2VAl to ~12 mW/mK^2 for Fe_2NbAl and Fe_2TaAl, and up to 16–20 mW/mK^2 for Fe_2NbGa, Fe_2TaGa, Fe_2NbIn, and Fe_2TaIn (Fig. 1 and Ref. [29], Fig. 4). Band-by-band analysis for Fe_2TaIn shows that most of the PF (90%) comes from the Fe e_g flat-and-dispersive band (Ref. [29], Fig. 6).

In a second set (S2) of Fe_2YZ compounds with Y = Ti, Zr, Hf and Z = Si, Ge, Sn, the dispersive Y e_g band is pushed up even higher in energy. It appears well above the Fe e_g bands, which are now the only lowest conduction bands (Fig. 1 and Ref. [29], Fig. 5). These compounds also exhibit extremely large PFs of ~14–17 mW/mK^2 at 300 K, consistent with what was reported in Ref. [60]. This time, the large PF is almost entirely generated by the Fe e_g flat-and-dispersive band [~93% of the total PF for Fe_2TiSn (Ref. [29], Fig. 6)].

In all S1 and S2 compounds exhibiting enhanced TE properties, the PF remains substantial (i.e., keeps 90% of its peak value) in a similar and relatively wide range of carrier concentrations ($n \approx 4 \times 10^{20}$ to 3×10^{21} cm^{-3}), at which $|S| \sim 150$–200 μV/K. These compounds then exhibit large S, comparable to those of Fe_2VAl and the best classical thermoelectrics, but at n and σ values that are about one order of magnitude larger (Ref. [29], Fig. 7).

Taking Fe_2TiSn as a representative example, the inspection of the carriers contributing to the transport properties at 300 K provides further insight into the enhancement of the PFs with respect to Fe_2VAl [Figs. 2(c) and 2(d)]. In the latter, the sizable TE properties at optimal doping arise from electrons located in small pockets centered at X and associated with highly dispersive V e_g bands [Fig. 2(c)]. In Fe_2TiSn, the enhanced transport properties at optimal doping are produced instead by electrons from the Fe e_g lowest conduction states located in three orthogonal tubes extending along Γ-X directions and intersecting at Γ [Fig. 2(d)]. These tubes can be viewed as the juxtaposition along the entire Γ-X direction of consecutive electron pockets similar to those of Fe_2VAl, thereby explaining the improved transport properties. This is an optimal realization of the concept of pocket engineering brought forward by Snyder *et al.* [61] where large S and σ values are obtained without compromising mobility by introducing degenerate low effective mass pockets in the Brillouin zone.

In each Cartesian direction, the Heusler Fe_2YZ structure can be seen as made of Fe_2 (alternating with YZ) atomic planes. For clarity, only the family of {001}-Fe_2 planes is illustrated in Fig. 2(a), but similar families can be drawn along the two other Cartesian directions. The tubular shape of the Fermi surface of Fe_2TiSn and related compounds is originating from the highly directional character of the Fe e_g orbitals. The conduction states of the three tubes in Fig. 2(d) are associated with the flat band along ΓX (and the symmetrically equivalent ΓY and ΓZ directions) in Fig. 1. For the tube along z, these states are made of Fe $d_{x^2-y^2}$ orbitals (see Ref. [29], Fig. 3) which strongly overlap in {001}-Fe_2 planes [strong σ^* bonds along x and y, Fig. 2(b)] but do not interact significantly from plane to plane (weak δ^* bonds along z). The same is true, *mutatis mutandis*, for the tubes along x and y. This anisotropy of the orbital interactions gives rise to electronic bands that are highly

dispersive in two directions ($m_t \sim 0.3m_e$ for Fe_2TiSn and $m_t \sim 0.2m_e$ for Fe_2TiSi) and flat in the third one ($m_l \sim 26m_e$ for Fe_2TiSn and $m_l \sim 90m_e$ for Fe_2TiSi), thereby concretizing the ideas of Mahan and Sofo [16]. The tubular shape of the Fermi surface comes from the large effective mass ratio ($R = m_l/m_t \sim 87$ for Fe_2TiSn and $R \sim 450$ for Fe_2TiSi) and highlights that these compounds exhibit a kind of two-dimensional electronic transport in Fe_2 planes [62], similar to what was proposed in nanostructures in order to realize increased TE performance [5]. Here, however, it is achieved in bulk cubic compounds. This yields a periodic repetition of two-dimensional conductive channels (i.e., Fe_2 planes) at the ultimate unit-cell scale. Moreover, the isotropic character of the properties is preserved through the coexistence of symmetry equivalent families of {001}-, {010}-, and {100}-Fe_2 planes. In practice, however, all of the conductive electrons are not similarly contributing to transport in a given direction: for instance, only the states in the tubes along x and y (the {100}- and {010}-Fe_2 planes) contribute significantly to the transport along z. All of this is a concrete illustration that low-dimensional electronic structures can occur in high-symmetry cubic systems, as also proposed recently by Parker *et al.* [23] for another class of compounds.

From the practical point of view, a central issue concerns the thermodynamical stability of the S1 and S2 compounds. This was investigated at the first-principle level (Ref. [29], text). The results are summarized in Fig. 2(e). Stable and unstable phases are associated with green and red colors, respectively. Compounds previously synthesized are stable. Fe_2TiGe and Fe_2NbGa with good TE performance are predicted to be fully stable. We see that including elements like In, Zr, or Hf with large ionic radii tends to destabilize the Heusler structure, although the synthesis of Fe_2HfSn might stay experimentally accessible. Another practical issue concerns the appearance of antisite defects in these Heusler compounds, which are detrimental to the TE performance [21]. From our calculations in Ref. [29], Table 2, S2 compounds appear to be less prone to form antisite defects than Fe_2VAl.

The existence of several isostructural stable compounds with very attractive PF is an advantage for TE applications. Combining such compounds in solid solutions should allow for the reduction of κ_l [9] while preserving the shape of their electronic band structure at the conduction band bottom (nearly identical since dominated by the same Fe e_g states, see Ref. [29], Fig. 5) and the related large PF. Such a reduction of κ_l has been demonstrated in $Fe_2V_{1-x}W_xAl$ alloys [58], reaching values of ~3 W/mK. The presence of heavier elements than V and Al is likely to lower κ_l of the new Heusler candidates compared to Fe_2VAl. In this context, reasonably low values can be expected, for instance, in Fe_2TiSn and its solid solutions (e.g., $Fe_2TiSn_{1-x}Si_x$). With $\kappa_l = 3.5$ W/mK, we estimate ZT values larger than 1 for Fe_2TiSn in the temperature range between 600–900 K (Ref. [29], Fig. 10). Such large ZT values are achieved at carrier concentrations only slightly lower than those corresponding to the optimum PF and at which S and n remain large. These ZT values are significantly larger than those predicted for Fe_2VAl, which properly reproduce the experiment ($ZT = 0.2$ at 400 K with $\kappa_l = 3.3$ W/mK, in agreement with Ref. [58]). This attests that the beneficial effect on the PF, achieved through the low-dimensional transport in Fe_2TiSn, can be accompanied by a significant increase of ZT without being systematically counterbalanced by another detrimental effect.

The excellent TE properties of some of the Fe_2YZ compounds demonstrated theoretically in this Letter, combined with the low-cost and wide availability of their constitutive elements, make them very attractive for large-scale TE applications, well beyond what could have been anticipated from previous studies of Fe_2VAl. Going further, our results also highlight that, contrary to current beliefs, extremely large PF can be intrinsic to bulk semiconductors. Our work rationalizes how this can be achieved in practice through the engineering of highly directional states at the bottom of the conduction bands, yielding low-dimensional transport. This calls for a search for alternative families of compounds realizing the same ideas. The link that we establish with some basic requirements on the electronic band structure is particularly relevant to succeed identifying such compounds in the current context of emergent high-throughput searches for alternative thermoelectrics [63,64] that require clear and simple design rules. Our findings might also attract interest well beyond the field of thermoelectrics: the singular Fermi surface in these systems presents close similarities to those of Fe-based superconductors [65] and the associated low-dimensional transport might be relevant in the context of some electronic [66] or photovoltaic [67] applications.

We thank P. Jacques, J.-P. Issi and N. Bristowe for useful discussions. Work supported by EnergyWall project CoGeTher, ARC project TheMoTherm, FNRS project HiT4FiT, and a collaboration between WBI and the Romanian Academy of Sciences. Ph.G. thanks a Research Professorship of the Francqui Foundation, D.I.B. the Romanian National Authority for Scientific Research, CNCS-UEFISCDI (Grant No. PN-II-RU-TE-2011-3-0085), G. H. and G.-M. R. the F.R.S.-FNRS and G. H. the European Marie Curie CIG (Grant No. HTforTCOs PCIG11-GA-2012-321988). Calculations were performed at Céci HPC Center, funded by F.R.S.-FNRS.

[1] T. M. Tritt and M. A. Subramanian, MRS Bull. **31**, 188 (2006).
[2] C. J. Vineis, A. Shakouri, A. Majumdar, and M. G. Kanatzidis, Adv. Mater. **22**, 3970 (2010).
[3] H. J. Goldsmid and R. W. Douglas, Br. J. Appl. Phys. **5**, 386 (1954).
[4] G. A. Slack, in *CRC Handbook Of Thermoelectrics* (CRC Press, Boca Raton, 1995), p. 407.
[5] L. D. Hicks and M. S. Dresselhaus, Phys. Rev. B **47**, 12727 (1993).

[6] G. Chen, M. S. Dresselhaus, G. Dresselhaus, J. P. Fleurial, and T. Caillat, Int. Mater. Rev. **48**, 45 (2003).
[7] J. G. Snyder and E. S. Toberer, Nat. Mater. **7**, 105 (2008).
[8] M. G. Kanatzidis, Chem. Mater. **22**, 648 (2010).
[9] K. Biswas, J. He, I. D. Blum, C.-I. Wu, T. P. Hogan, D. N. Seidman, V. P. Dravid, and M. G. Kanatzidis, Nature (London) **489**, 414 (2012).
[10] R. Venkatasubramanian, E. Siivola, V. Colpitts, and B. O'Quinn, Nature (London) **413**, 597 (2001).
[11] T. C. Harman, P. J. Taylor, M. P. Walsh, and B. E. LaForge, Science **297**, 2229 (2002).
[12] K. F. Hsu *et al.*, Science **303**, 818 (2004).
[13] J. P. Heremans, M. S. Dresselhaus, L. E. Bell, and D. T. Morelli, Nat. Nanotechnol. **8**, 471 (2013).
[14] L. D. Hicks, T. C. Harman, X. Sun, and M. S. Dresselhaus, Phys. Rev. B **53**, R10493 (1996).
[15] H. Ohta *et al.*, Nat. Mater. **6**, 129 (2007).
[16] G. D. Mahan and J. O. Sofo, Proc. Natl. Acad. Sci. U.S.A. **93**, 7436 (1996).
[17] D. M. Rowe, V. L. Kuznetsov, L. A. Kuznetsova, and G. Min, J. Phys. D **35**, 2183 (2002).
[18] D. Bilc, S. Mahanti, E. Quarez, K.-F. Hsu, R. Pcionek, and M. Kanatzidis, Phys. Rev. Lett. **93**, 146403 (2004).
[19] S. Ahmad, K. Hoang, and S. D. Mahanti, Phys. Rev. Lett. **96**, 056403 (2006).
[20] J. P. Heremans, V. Jovovic, E. S. Toberer, A. Saramat, K. Kurosaki, A. Charoenphakdee, S. Yamanaka, and G. J. Snyder, Science **321**, 554 (2008).
[21] D. I. Bilc and P. Ghosez, Phys. Rev. B **83**, 205204 (2011).
[22] B. Paul, P. K. Rawat, and P. Banerji, Appl. Phys. Lett. **98**, 262101 (2011).
[23] D. Parker, X. Chen, and D. J. Singh, Phys. Rev. Lett. **110**, 146601 (2013).
[24] Y. Nishino, S. Deguchi, and U. Mizutani, Phys. Rev. B **74**, 115115 (2006).
[25] R. Dovesi, R. Orlando, B. Civalleri, C. Roetti, V. R. Saunders, and C. M. Zicovich-Wilson, Z. Kristallogr. **220**, 571 (2005).
[26] D. I. Bilc, R. Orlando, R. Shaltaf, G.-M. Rignanese, J. Íñiguez, and Ph. Ghosez, Phys. Rev. B **77**, 165107 (2008).
[27] G. K. H. Madsen and D. J. Singh, Comput. Phys. Commun. **175**, 67 (2006).
[28] M. Vasundhara, V. Srinivas, and V. V. Rao, Phys. Rev. B **77**, 224415 (2008).
[29] See Supplemental Material at http://link.aps.org/supplemental/10.1103/PhysRevLett.114.136601, which includes Refs. [30–52], for further technical details and data supporting our results.
[30] I. de P. R. Moreira, R. Dovesi, C. Roetti, V. R. Saunders, and R. Orlando, Phys. Rev. B **62**, 7816 (2000).
[31] E. Ruiz, M. Llunell, and P. Alemany, J. Solid State Chem. **176**, 400 (2003).
[32] R. Pandey, M. Causa, N. M. Harrison, and M. Seel, J. Phys. Condens. Matter **8**, 3993 (1996).
[33] T. Bredow, P. Heitjans, and M. Wilkening, Phys. Rev. B **70**, 115111 (2004).
[34] D. Munoz-Ramo, J. L. Gavartin, and A. L. Shluger, Phys. Rev. B **75**, 205336 (2007).
[35] A. R. Porter, M. D. Towler, and R. J. Needs, Phys. Rev. B **60**, 13534 (1999).
[36] Z. Wu and R. E. Cohen, Phys. Rev. B **73**, 235116 (2006).
[37] A. D. Becke, J. Chem. Phys. **104**, 1040 (1996).
[38] M. Goffinet, P. Hermet, D. I. Bilc, and Ph. Ghosez, Phys. Rev. B **79**, 014403 (2009).
[39] A. Prikockytė, D. Bilc, P. Hermet, C. Dubourdieu, and P. Ghosez, Phys. Rev. B **84**, 214301 (2011).
[40] Y. Feng, J. Rhee, T. Wiener, D. Lynch, B. Hubbard, A. Sievers, D. Schlagel, T. Lograsso, and L. Miller, Phys. Rev. B **63**, 165109 (2001).
[41] S. Dordevic, D. Basov, A. Ślebarski, M. Maple, and L. Degiorgi, Phys. Rev. B **66**, 075122 (2002).
[42] P. Blaha *et al.*, *WIEN2k: An Augmented Plane Wave Plus Local Orbitals Program for Calculating Crystal Properties* (Vienna University of Technology, Vienna, 2001).
[43] D. J. Singh and I. I. Mazin, Phys. Rev. B **57**, 14352 (1998).
[44] C. S. Lue and Y.-K. Kuo, J. Appl. Phys. **96**, 2681 (2004).
[45] A. Popescu, L. M. Woods, J. Martin, and G. S. Nolas, Phys. Rev. B **79**, 205302 (2009).
[46] H. Chen, G. Hautier, and G. Ceder, J. Am. Chem. Soc. **134**, 19619 (2012).
[47] G. Hautier, S. Ping Ong, A. Jain, C. J. Moore, and G. Ceder, Phys. Rev. B **85**, 155208 (2012).
[48] Y. Nishino, M. Kato, S. Asano, K. Soda, M. Hayasaki, and U. Mizutani, Phys. Rev. Lett. **79**, 1909 (1997).
[49] C. S. Lue, J. H. Ross, K. D. D. Rathnayaka, D. G. Naugle, S. Y. Wu, and W.-H. Li, J. Phys. Condens. Matter **13**, 1585 (2001).
[50] C. Lue, R. Liu, M. Song, K. Wu, and Y. Kuo, Phys. Rev. B **78**, 165117 (2008).
[51] A. Ślebarski and J. Goraus, Phys. Rev. B **80**, 235121 (2009).
[52] M. Perrier, A. Deschamps, O. Bouaziz, Y. Brechet, F. Danoix, F. De Geuser, P. Donnadieu, K. Hoummada, and P. Maugis, Metall. Mater. Trans. A **43**, 4999 (2012).
[53] G. Kresse and J. Furthmüller, Comput. Mater. Sci. **6**, 15 (1996).
[54] J. P. Perdew, K. Burke, and M. Ernzerhof, Phys. Rev. Lett. **77**, 3865 (1996).
[55] Materials Project, http://www.materialsproject.org.
[56] A. Jain, G. Hautier, C. J. Moore, S. Ping Ong, C. C. Fischer, T. Mueller, K. A. Persson, and G. Ceder, Comput. Mater. Sci. **50**, 2295 (2011).
[57] S. Ping Ong, W. Davidson Richards, A. Jain, G. Hautier, M. Kocher, S. Cholia, D. Gunter, V. L. Chevrier, K. A. Persson, and G. Ceder, Comput. Mater. Sci. **68**, 314 (2013).
[58] M. Mikami, Y. Kinemuchi, K. Ozaki, Y. Terazawa, and T. Takeuch, J. Appl. Phys. **111**, 093710 (2012).
[59] M. Mikami, K. Kobayashi, T. Kawada, K. Kubo, and N. Uchiyama, J. Electron. Mater. **38**, 1121 (2009).
[60] S. Yabuuchi, M. Okamoto, A. Nishide, Y. Kurosaki, and J. Hayakawa, Appl. Phys. Express **6**, 025504 (2013).
[61] Y. Pei, X. Shi, A. Lalonde, H. Wang, L. Chen, and G. J. Snyder, Nature (London) **473**, 66 (2011).
[62] The 1D shape of a Fermi surface is associated with 2D transport in real space. Because of the orientation of the $d_{x^2-y^2}$ orbitals, the latter can be viewed as the combination of two orthogonal transport channels along the Fe-Fe bonds.
[63] S. Wang, Z. Wang, W. Setyawan, N. Mingo, and S. Curtarolo, Phys. Rev. X **1**, 021012 (2011).
[64] I. Opahle, G. K. H. Madsen, and R. Drautz, Phys. Chem. Chem. Phys. **14**, 16197 (2012).
[65] D. J. Singh, Sci. Tech. Adv. Mater. **13**, 054304 (2012).
[66] Y. Z. Chen *et al.*, Nat. Commun. **4**, 1371 (2013).
[67] A. Tebano, E. Fabbri, D. Pergolesi, G. Balestrino, and E. Traversa, ACS Nano **6**, 1278 (2012).

Supplemental Material – Low-dimensional transport and large thermoelectric power factors in bulk semiconductors by band engineering of highly-directional electronic states

1 Electronic and thermoelectric properties

1.1 Technical details

The electronic properties were studied using the linear combination of atomic orbitals (LCAO) method and localized Gaussian basis sets as implemented in CRYSTAL. [1] The basis sets used are: Fe [2], V [3], 976-31(631d) for Nb [4], 11(31d) for Ta [5], 88-31 with the optimized outermost gaussian exponent sp=0.1 for Al [4], Ga [6], 976-311(631d) for In [4], Ti [7], 976-31(621d) for Zr [5], Hf [8], Si [9], Ge [3], and 976-3111(631d) with the outermost gaussian exponent sp=0.1053 for Sn [4]. The outermost two sp and one d gaussian exponents of Fe, and V, and the outermost sp exponent of Al were optimized in Fe_2VAl. Their respective values are: 1.155, 0.2817, 0.2439, 0.8335, 0.1151, 0.338, and 0.1. Effective core pseudopotentials were considered for Ta and Hf. The other elements were treated at the all electron level. We use a hybrid functional approach, B1-WC [10], which mixes the generalized gradient approximation functional of Wu and Cohen [11] with 16% of exact exchange within the B1 scheme. [12] B1-WC describes accurately the electronic and TE properties of this class of compounds [13], and is more appropriate to treat d and f electronic materials, being a good alternative to LDA(GGA)+U [14, 15].

Other technical details are as follows. The optimized lattice constants were determined considering a 9x9x9 mesh of k points in the Brillouin zone of the fcc cell, and the self-consistent calculations were considered to be converged when the energy changes between interactions were smaller than 10^{-8} Hartree. An extralarge predefined pruned grid consisting of 75 radial points and 974 angular points was used for the numerical integration of charge density. The level of accuracy in evaluating the Coulomb and exchange series is controlled by five parameters. [1] Their values used in our calculations are 7, 7, 7, 7, and 14.

The electronic transport calculations were performed within the Boltzmann transport formalism and the constant relaxation-time approximation using BoltzTraP code. [16] In Boltzmann transport formalism, the electrical conductivity, thermopower, and electronic thermal conductivity tensors are estimated as:

$$\overleftrightarrow{\sigma} = \frac{e^2}{\Omega} \sum_{i\vec{k}} \left(-\frac{\partial f_\mu(T, E_{i\vec{k}})}{\partial E_{i\vec{k}}} \right) \tau(T, E_{i\vec{k}}) \vec{v}_{i\vec{k}} \vec{v}_{i\vec{k}} \tag{1}$$

$$\overleftrightarrow{S} = \frac{-|e|}{\Omega T \overleftrightarrow{\sigma}} \sum_{i\vec{k}} \left(-\frac{\partial f_\mu(T, E_{i\vec{k}})}{\partial E_{i\vec{k}}} \right) (E_{i\vec{k}} - \mu) \tau(T, E_{i\vec{k}}) \vec{v}_{i\vec{k}} \vec{v}_{i\vec{k}} \tag{2}$$

$$\overleftrightarrow{\kappa}^0 = \frac{1}{\Omega T}\sum_{i\vec{k}}\left(-\frac{\partial f_\mu(T,E_{i\vec{k}})}{\partial E_{i\vec{k}}}\right)(E_{i\vec{k}}-\mu)^2\tau(T,E_{i\vec{k}})\vec{v}_{i\vec{k}}\vec{v}_{i\vec{k}} \quad (3)$$

$$\vec{v}_{i\vec{k}} = \frac{1}{\hbar}\frac{\partial E_{i\vec{k}}}{\partial \vec{k}} \quad (4)$$

where e is electronic charge, Ω is unit cell volume, f_μ is Fermi distribution function, τ is relaxation time, $E_{i\vec{k}}$ are electronic energies and $\vec{v}_{i\vec{k}}$ are particles velocities of the i-th electronic band at each $\vec{k}$ vector from the reciprocal space. In the constant relaxation time approximation τ is considered as a constant, $\tau(T,E_{i\vec{k}}) = \tau_0$, and in this approximation the thermopower tensor $\overleftrightarrow{S}$ is independent of τ_0. $\overleftrightarrow{\kappa}^0$ is the tensor of electronic thermal conductivity at zero electric field. For the cubic symmetry only the diagonal components of the tensors are finite and $\sigma_{xx} = \sigma_{yy} = \sigma_{zz} = \sigma$, $S_{xx} = S_{yy} = S_{zz} = S$, $\kappa^0_{xx} = \kappa^0_{yy} = \kappa^0_{zz} = \kappa^0$.

For the transport calculations, the electronic charge density was first converged considering denser 14x14x14 k-point meshes in the Brillouin zone and the energy convergence was increased to 10^{-10} Hartree. Using this charge density then, the transport coefficients were very well converged for the electronic energies calculated on very dense 61x61x61 k-point meshes. The relaxation time τ_0=3.4x10^{-14} s was determined by fitting the experimental electrical resistivity ρ=0.65 mΩcm of $Fe_2VAl_{1-x}M_x$ (M = Si, Ge) systems at doping x=0.03 and 300 K. [17, 18] Assuming that each atom M brings one additional electron, this corresponds to a total electron concentration $n_{tot}\sim$6x10^{20} cm^{-3}, which include also the extrinsic contribution of holes $n_h\sim$5x10^{20} cm^{-3}. Therefore, we estimated τ_0 by fitting the theoretical value of ρ at 300 K and intrinsic electron concentration $n\sim$7x10^{19} cm^{-3} (value for which the maximum n-type PF is achieved) with the experimental value of 0.65 mΩcm. Using this value of τ_0, the calculated PF of Fe_2VAl at 300 K is $\sim$3 mWm^{-1}K^{-2}, which underestimates the experimental PF=4-6 mWm^{-1}K^{-2}. [17, 18]

1.2 Reasoning for using the same relaxation time in Fe_2YZ compounds

By using the same relaxation time in a given class of materials, such as Fe_2YZ Heusler compounds, one can identify the optimum electronic band structure, which can qualitatively maximize PF's from the point of view of the electronic and transport properties. More over, the transport in this class of compounds is achieved through the same d e_g electronic states (Y and Fe d e_g bands), having similar light effective masses m_t which contribute in a given orthogonal transport direction.

The very large PF's of Fe_2YZ are achieved through a low-dimensional electronic transport in the Fe-Fe atomic planes, yielding periodic conductive channels at the atomic scale, which maximizes n. The electrons are highly mobile in the Fe-Fe atomic planes with the effective masses $m_t\sim$0.2-0.3 m_e, and very heavy with effective masses $m_l\sim$26-90 m_e from one Fe-Fe plane to the next. This give rise to three orthogonal tubes in inverse space along the orthogonal cubic axes with the light m_t transverse to the tubes and heavy m_l along the tubes. In Fe_2VAl the three electronic pockets located at X points, which participate in transport have the light m_t=0.35 m_e

and heavy m_l=0.7 m_e effective mass values. In a given transport orthogonal direction only the two tubes and two pockets with light m_t in the transport direction will contribute significantly to the transport. Comparing the light m_t values, we see that the compounds exhibiting very large PF's possess more mobile electrons in transport. This is consistent with having large electron mobilities μ in the low-dimensional transport systems.

Further evidence for the electron mobility μ and τ_0 can be extracted from the optical conductivities of Fe_2VAl [19] and Fe_2TiSn [20] probed by infrared and optical spectroscopy. In Fe_2VAl, the mean free path of electrons l (l=$v_F\tau_0$, v_F is Fermi velocity) has a very small value of 24 $\AA$ at 300K. [19] Because of large atomic disorder and small l, the estimated relaxation time τ_0 values are $\sim$1x10^{-14} s at 300K and do not depend significantly on the sample carrier densities of Fe_2VAl. [19] The alloying at Al site decrease the residual resistivity and disorder of Fe_2VAl. [17, 18, 19] The residual resistivity value of $\sim$2.5 mΩcm of Fe_2VAl is decreased to $\sim$0.5 mΩcm in the $Fe_2VAl_{1-x}Ge_x$ system at doping x=0.03, explaining the larger τ_0 value of 3.4x10^{-14} s estimated from electrical resistivity measurements. [17] On the other hand in Fe_2TiSn, the mean free path of electrons l has a much larger value of 80 $\AA$ at 300K. [20] Using the carrier density n=5x10^{20} cm^{-3} (n=$k_F{}^3$/(3π^2), k_F is Fermi k vector) and l=80 $\AA$ values, we estimate τ_0 to be 2.8x10^{-14} s at 300K, which is comparable with the 3.4x10^{-14} s value used in our transport calculations. These results are consistent with our findings which show the compounds from S2 set to be less prone to have disorder than those from S1 set.

The above relaxation times were estimated considering free electronic metallic behavior. If we consider the doped semiconducting behavior then the electrons reside inside three idealized Fermi spheres for Fe_2VAl and three idealized cylinders for Fe_2TiSn (low-dimensional transport). Then we have:

$$n = \frac{2*3}{(2\pi)^3}\frac{4\pi}{3}k_F^3; n = \frac{1}{\pi^2}k_F^3; \qquad \text{for } Fe_2VAl$$

$$n = \frac{2*3}{(2\pi)^3}\frac{2\pi}{a}\pi k_F^2; n = \frac{3}{2\pi a}k_F^2; \quad \text{for } Fe_2TiSn$$

$$\tau_0 = \frac{l}{\frac{\hbar}{m_e}k_F}$$

where 2 and 3 in the nominator stands for electronic spin and pocket degeneracy, and a is the lattice constant of Fe_2TiSn cubic cell. Using the above expressions for n and τ_0, the estimated relaxation time for Fe_2VAl is $\tau_0\sim$1.2-1.6x10^{-14} s. These values are larger than the values $\tau_0\sim$1x10^{-14} s estimated in Ref. [19]. For Fe_2TiSn at n=5x10^{20} cm^{-3}, the relaxation time is $\tau_0\sim$8.75x10^{-14} s, which is $\sim$2.6 times larger then the used value. This is an indication that the relaxation time τ_0 and electron mobilities μ in low-dimensional transport systems can be much larger than in 3-dimensional transport systems. These results are supported also by the very large electron mobilities achieved in low-demensional transport systems such as: two-dimensional electron gas (2DEG), carbon nonotubes and BN graphene at room temperature. In 2DEG the electron mobilities can be even higher than those of the bulk constituents.

From all these arguments, we believe that the 4-5 fold increase in the PF's of Fe_2YZ Heusler compounds which exhibit low-dimensional transport with respect to classical thermoelectrics has physical grounds and is not an artifact of a very large relaxation time used in the transport calculations. If the electron mobilities are comparable or larger than those of classical thermoelectrics, then an increase of 10 fold or greater can be expected in PF's of these materials.

1.3 Role of spin-orbit interactions

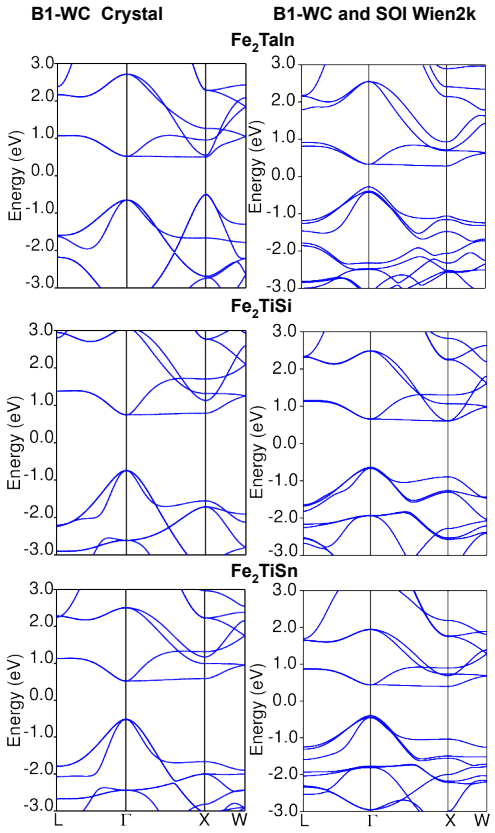

Figure 1: Electronic band structures: within B1-WC full hybrid using CRYSTAL code in the left column and within B1-WC partial hybrid including spin-orbit interactions (SOI) using WIEN2K code in the right column. The splitting of the degenerate bands is due to SOI interactions.

In order to check the effect of spin-orbit interactions (SOI) and the robustness of these extremely large PF's, we used also the augmented plane wave and local orbital (APW + lo) method as implemented in WIEN2K code. [21] These calculations were performed within the partial implementation of B1-WC hybrid functional. In the WIEN2K and APW + lo method the hybrid functionals are implemented only inside of augmented-plane-wave spheres around the

atoms. These radii were taken to be 2.2 Bohr for all atoms. The scalar relativistic effects were also included. The self-consistent iterations were performed for a 14x14x14 k-point meshes inside of the Brillouin zone (BZ) to within 0.0001 Ry. The number of plane waves is defined by RK_{max} whereas the largest vector in the charge-density Fourier expansion is defined by G_{max}, which were taken to be 9 and 16, respectively. The transport properties were estimated also for very dense 49x49x49 k-point meshes. A larger value of relaxation time τ_0=3.4x10^{-14} s was estimated in the same way fitting the experimental ρ=0.65 mΩcm at intrinsic electron concentration $n\sim$7x10^{19} cm^{-3} and 300 K. [13] The estimated PF of Fe_2VAl at 300 K is $\sim$3 mWm^{-1}K^{-2} using τ_0=3.4x10^{-14} s.

The SOI effect on the electronic band structure of these Fe based full Heusler compounds is not very significant. The SOI splits the degenerate top valence and bottom conduction bands, but it does not shift in energy the position of the very flat band along ΓX direction of the Brillowin zone (BZ) (see Figures 1). The difference in the position of the dispersive band at X point are due to the partial hybrid implementation of B1-WC within WIEN2K code, in which the electronic properties outside augmented-plane-wave spheres are described within the GGA of Wu and Cohen. [11]

1.4 Electronic band structure

As clarified recently [13], Fe_2VAl is an intrinsic semiconductor, with a low band-gap between highest conduction bands of dominant Fe t_{2g} character and a highly dispersive lowest conduction band of dominant V e_g character. The electronic band structure of Fe_2VAl was previously interpreted by Singh and Mazin [22]. On the one hand, the splitting of V d levels into occupied V t_{2g} states lying $\sim$-2 eV below the Fermi energy and empty V e_g states forming the lowest conduction band is mainly due to the octahedral crystal field produced by the bcc-like coordination of the V site. On the other hand, the Fe d levels are split such that all of these states, except Fe e_g anti-bonding, are lying in the valence band. The highest valence bands have a dominant Fe t_{2g} character while the Fe e_g anti-bonding states are located about 0.6 eV above the conduction band bottom. In this case, the splitting is no more driven by the crystal field but by the strength of the Fe-Fe hybridizations. This description is fully supported by the orbital character analysis reported in Fig. 2 (calculations performed using WIEN2K code within B1-WC partial hybrid and including SOI).

The engineering of the positions of Fe e_g and Y e_g conduction states from atomic substitutions at the Y and Z sites can be globally interpreted from the following dominant arguments. On the one hand, going from $3d$ to $5d$ elements at the Y site tends to move up the Y e_g higly-dispersive band. On the other hand, considering bigger elements at Y and Z sites increases the lattice parameter and therefore the Fe-Fe interatomic distance; this results in a decrease of Fe-Fe interactions lowering the splitting between occupied Fe t_{2g} and unoccupied Fe e_g states and so moving down the flat-and-dispersive Fe e_g levels. Consequently, in many compounds, the Fe e_g flat-and-dispersive band appears at or close to the bottom of the conduction band (see Figures 4, and 5). At Γ , the two Fe e_g levels ($d_{x^2-y^2}$ and d_{z^2}) are degenerated by symmetry; when moving

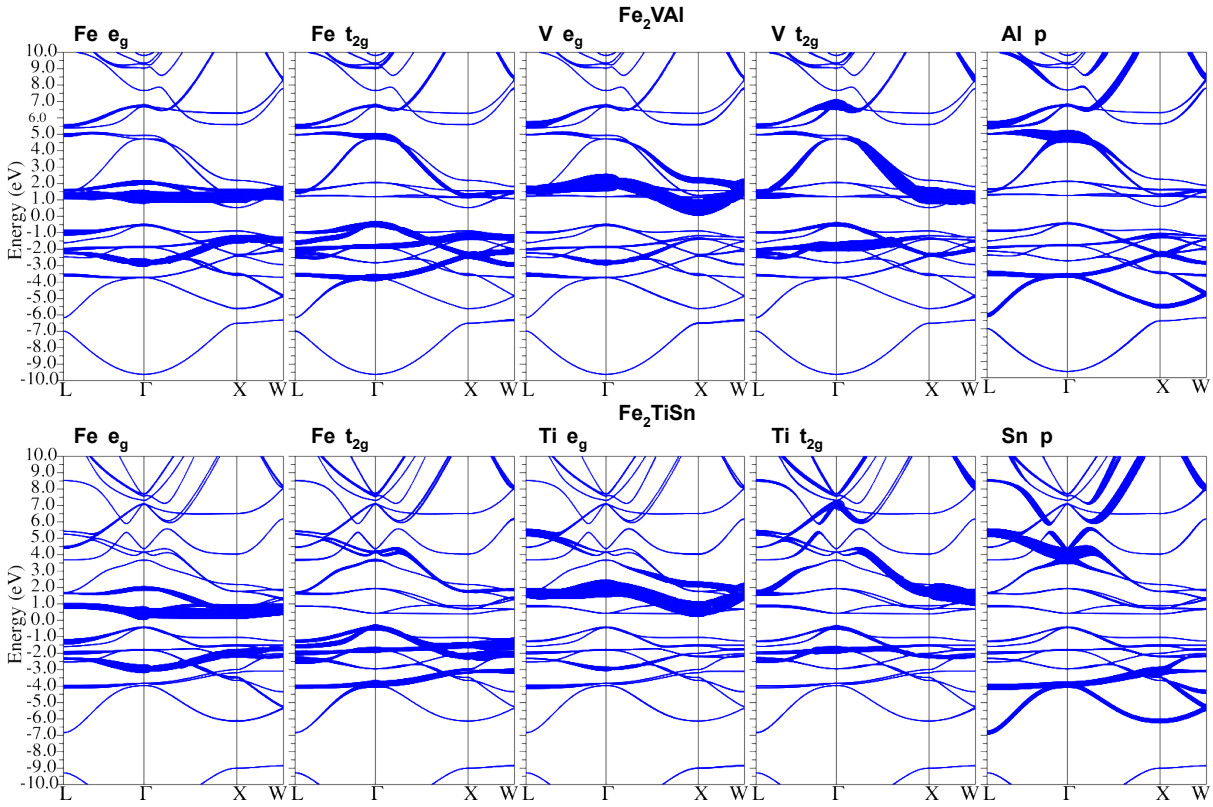

Figure 2: Orbital character of the band structure of Fe_2VAl and Fe_2TiSn within B1-WC partial hybrid including spin-orbit interactions (SOI) using WIEN2K code. The size of the circles (thick plotting) is proportional with the orbital character of the bands.

along one of the equivalent ΓX, ΓY or ΓZ direction, the degeneracy is lifted. As illustrated in Fig. 3, along ΓZ, the flat e_g band corresponds to $d_{x^2-y^2}$ levels and the dispersive one to d_{z^2} levels. This is related to the fact that $d_{x^2-y^2}$ orbitals strongly overlap in the $\{001\}$-Fe_2 plane (σ^* bonds along x and y directions) and do not interact much between consecutive planes along z (eventual weak δ^* bonds). The same is true, *mutatis mutandis*, along ΓX and ΓY directions.

1.5 Thermoelectric properties

The very large n-type PF's are generated by the narrow energy distribution of the flat Fe e_g band along ΓX direction (see Figures 1, 4, and 5). The analysis of band contribution to PF's of Fe_2TaIn, Fe_2TiSi and Fe_2TiSn, indeed shows that the flat-and-dispersive Fe e_g band contributes 90 %, 94 %, and 93 % to total PF, respectively (see Figure 6).

Although there are some differences in the electronic band structure of the compounds due to the partial hybrid implementation of B1-WC, we estimate in both methods (LCAO and APW + lo) the very large n-type PF's (see Figures 1, and 6). This supports the robustness of the

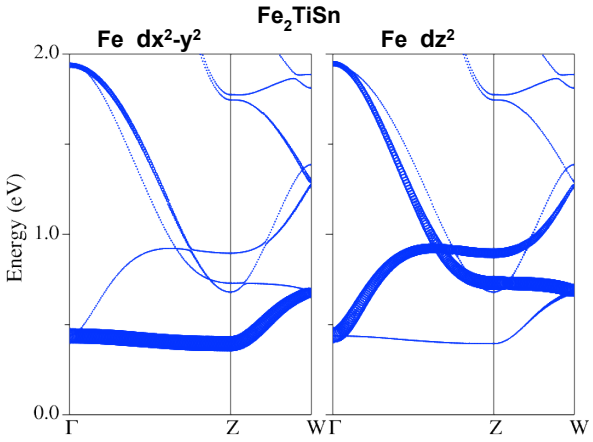

Figure 3: Fe $d_{x^2-y^2}$ and d_{z^2} orbital character of Fe_2TiSn band structure within B1-WC partial hybrid including spin-orbit interactions (SOI) using WIEN2K code. The size of the circles (thick plotting) is proportional with the orbital character of the bands.

results, and moreover the large n-type PF's are not affected by the SOI interactions.

It is interesting to identify the individual contributions of thermopower S and electrical conductivity σ to the very large n-type PF (see Figure 7). The presence in the bottom of the conduction band of the flat-and-dispersive Fe e_g band which is very flat along ΓX direction and dispersive in the transverse directions of BZ allows S values which are comparable with those of classical thermoelectrics (such as PbTe or Bi_2Te_3), but at much larger n and σ values.

We further notice that the PF we get at room temperature in Heusler compounds are comparable to those achieved in rare-earth compounds like $YbAl_3$ that exhibit amongst the highest ever reported PF (in the latter, S is twice smaller and σ four times larger) [23]. $YbAl_3$ and related compounds are however metals : they exhibit relatively low ZT (0.2 at 300 K in $YbAl_3$) and their interesting TE properties are rapidly destroyed when increasing temperature (PF $\sim$7 mW/mK^2 in $YbAl_3$ at 600K). In contrast, the Heusler compounds are semiconductors; their PF increases with increasing temperature (PF$\sim$26 mW/mK^2 in Fe_2TiSn at 600K) and, as it is discussed below, they are expected to yield ZT values attractive for applications at appropriate operating temperatures.

It is important to estimate what ZT values can yield the large PF's obtained in Heusler compounds, specially because these PF's are achieved at large n and σ values (compared to classical thermoelectrics). In order to estimate the figure of merit ZT :

$$ZT = \frac{\sigma S^2}{\kappa_l + \kappa_e} T \tag{5}$$

we need to access the electronic κ_e and lattice κ_l thermal conductivities. κ_e can be estimated through Wiedemann-Franz law $\kappa_e = L_0 \sigma T$, where $L_0 = 2.45 \times 10^{-8}$ WΩ/K^2 is the Lorenz number, but also from our first-principles calculations as [16]:

$$\kappa_e = \kappa^0 - \sigma S^2 T \tag{6}$$

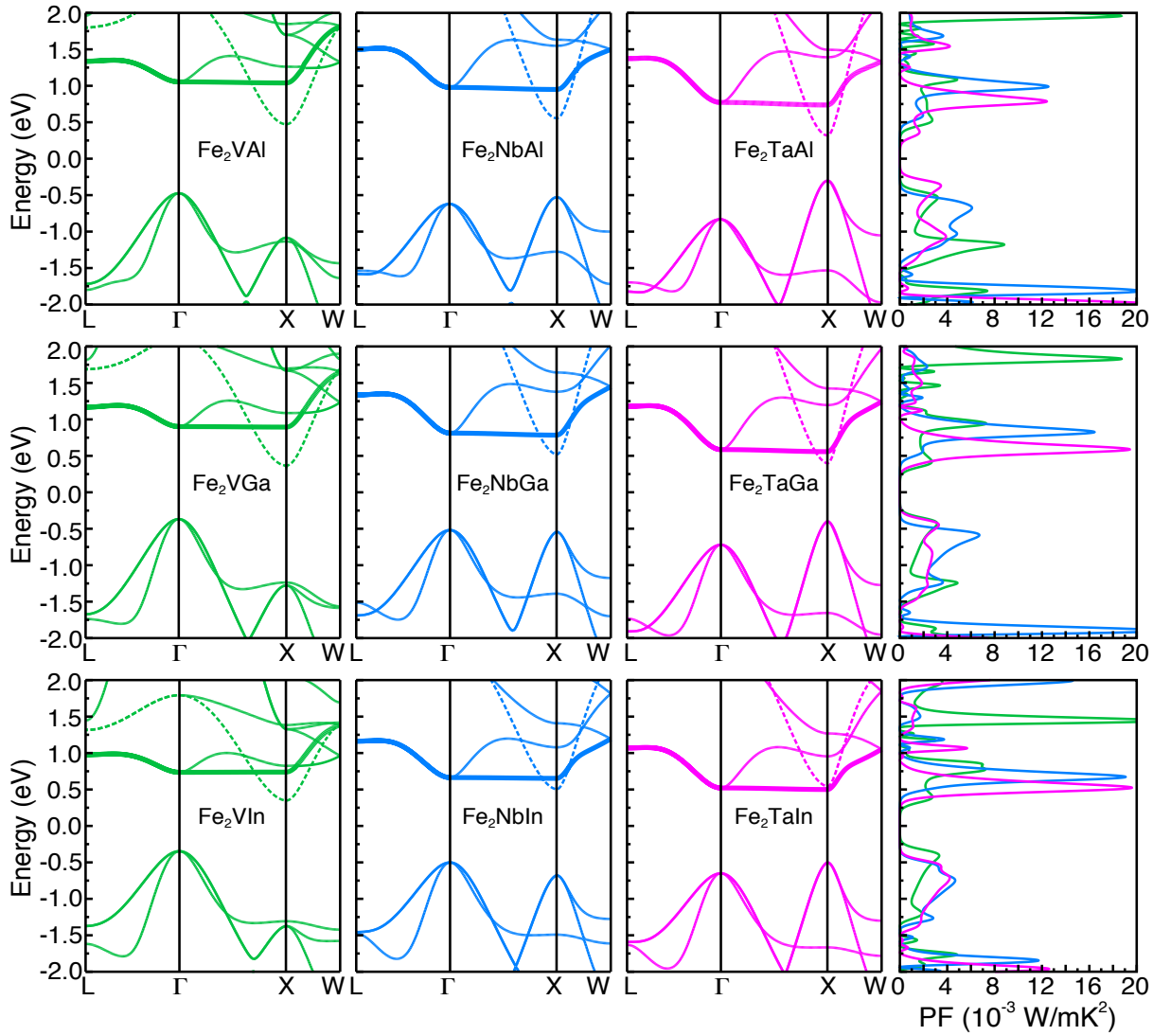

Figure 4: Electronic band structures and power factors (PF=$S^2\sigma$) for the set S1 of compounds. Fe_2YZ full Heusler compounds with Y=V (green), Nb (blue), Ta (magenta) and Z=Al, Ga, In (1^{st}, 2^{nd}, and 3^{rd} row, respectively). Dotted lines indicate the highly-dispersive lowest conduction band of dominant Y e_g character. The bold lines shows the band of Fe e_g character that is flat along the ΓX direction and highly-dispersive along others.

where κ^0 is the electronic thermal conductivity at zero electric field, accessible in BoltzTraP code (in our calculations, we assume the same relaxation time for σ and κ_e). This means that, from our calculations, we can estimate the Lorentz function L (independent of τ_0 within the

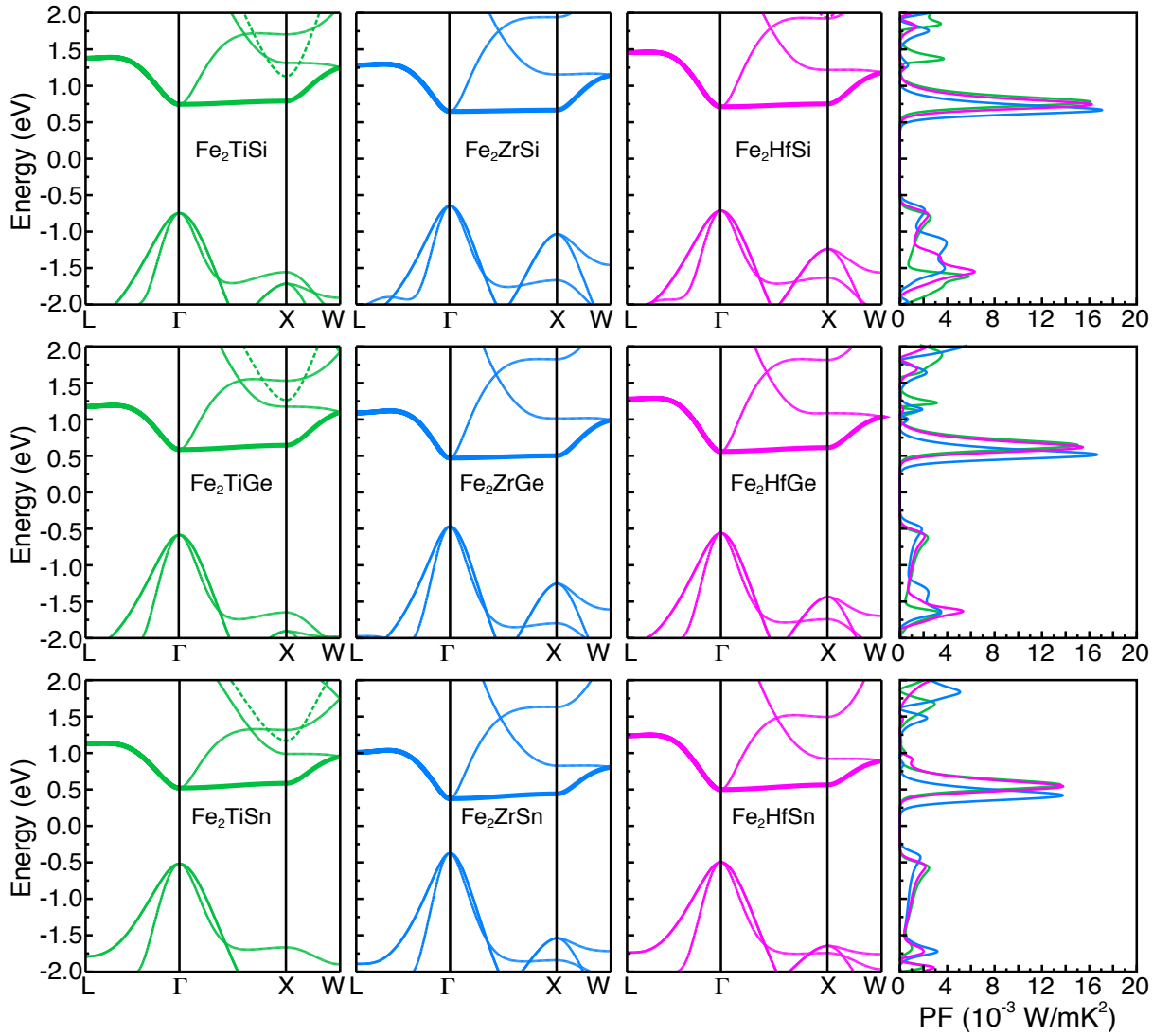

Figure 5: Electronic band structures and power factors (PF=$S^2\sigma$) for the set S2 of compounds. Fe_2YZ full Heusler compounds with Y=Ti (green), Zr (blue), Hf (magenta), and Z=Si, Ge, Sn (1^{st}, 2^{nd}, and 3^{rd} row, respectively). Same conventions as in Figure 1.

constant relaxation time approximation) as:

$$L = \frac{\kappa^0}{\sigma T} - S^2 \tag{7}$$

At the optimized values of the ZT (see below), L is smaller than L_0 by $\sim$20% in Fe_2VAl (see Figure 8, and Table 1). The L_0 limit is achieved at large electronic concentrations in the metallic regime. For Fe_2TiSn, L is strongly decreased by $\sim$29% ($\sim$51%) at 300K (900K) even

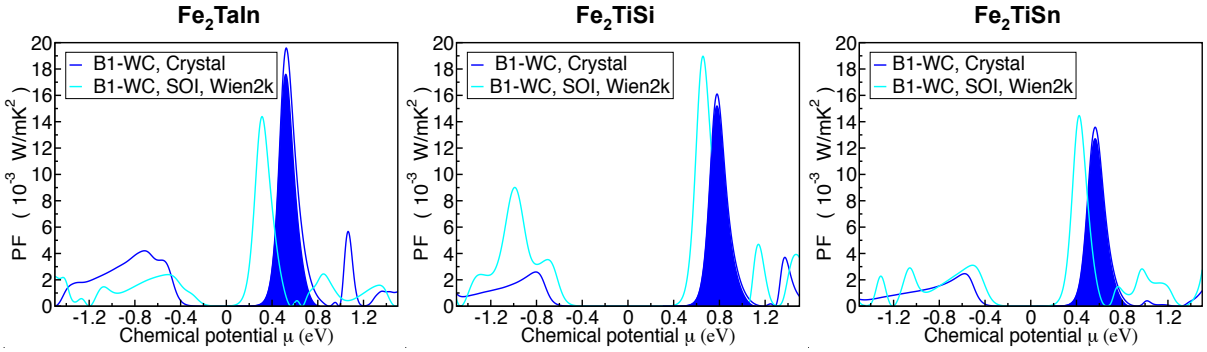

Figure 6: Power factors PF=σS^2 dependence on chemical potential μ at 300 K within B1-WC full hybrid using CRYSTAL code and within B1-WC partial hybrid including spin-orbit interactions (SOI) using WIEN2K code. The flat-and-dispersive band contribution to the PF's estimated within B1-WC full hybrid is shown in background blue color. The positions of the extremely large PF's differ because of the differences in the band gaps for the two types of calculations.

though the electronic concentrations are about one order of magnitude larger than in Fe_2VAl. This means that κ_e will be significantly smaller than expected from the Wiedemann-Franz law.

In first approximation, ZT can be estimated within the constant relaxation time approximation, using some reasonable expected values of κ_l. Recently, a low value of κ_l∼3.3 W/mK was obtained in $Fe_2V_{0.9}W_{0.1}Al$ alloys [24], yielding a ZT∼0.2 at 400K. The κ_l of Fe_2TiSn is ∼7 W/mK at 300K [25]. Therefore, in this family of compounds, reasonably low values of κ_l∼3 W/mK are expected to be achieved through alloying, and even lower values through nanostructuring. The estimated ZTs using different κ_l values at three different temperatures are shown in Fig. 9, and the TE properties obtained at the optimized ZT's are given in Table 1. ZT values up to 2 are estimated for these compounds using realistic κ_l values of ∼3.5 W/mK in 300-600K intermediate temperature range.

However, the constant relaxation time approximation will inevitably provide unrealistically large ZT values at high temperature, where phonon scattering becomes important. In order to provide more accurate estimate of ZT, we went so beyond the constant relaxation time approximation and considered the temperature T and energy E_k dependences of the relaxation time $\tau(T, E_k)$ for the acoustic and polar optical phonon scattering mechanisms. $\tau(T, E_k)$ is determined from electron-phonon interactions as:

$$\frac{1}{\tau(T, E_k)} = \sum_{\vec{k'} \neq \vec{k}} P_{\vec{k'}\vec{k}} \tag{8}$$

where $P_{\vec{k'}\vec{k}}$ is the scattering probability of an electron with vector $\vec{k}$ to be scattered in another state $\vec{k'}$ and the sum is over all final states $\vec{k'}$. During the scattering processes the wave vector $\vec{k'} = \vec{k} \pm \vec{q}$ and energy $E_{k'} = E_k \pm \hbar\omega_q$ are conserved, where $\vec{q}$ and ω_q are the phonon wave

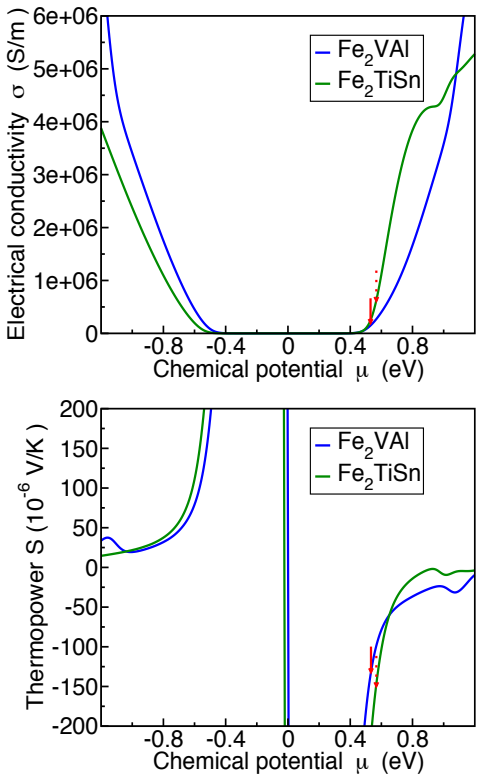

Figure 7: Electrical conductivity σ and thermopower S dependence on chemical potential μ of Fe_2VAl and Fe_2TiSn at 300 K. The solid red arrows indicate $\sigma\sim$155x10^3 S/m and $S\sim$ -133 μV/K at n = 9x10^{19} cm^{-3}, whereas dotted red lines indicate $\sigma\sim$587x10^3 S/m and $S\sim$ -152 μV/K at n = 1x10^{21} cm^{-3}.

vector and mode frequency, respectively. In the limit of small $\vec{q} \to 0$, the scattering by acoustic phonons is nearly elastic $\omega_q \to 0$, whereas optical phonon scattering is inelastic and the dispersion of long-wavelength optical phonons near the zone center ($\vec{q} \to 0$) is very flat and one can assume that $\omega_q = \omega_{LO}$, where ω_{LO} is the longitudinal optical mode frequency. $P_{\vec{k'}\vec{k}}$ can be estimated by Fermi's golden rule:

$$P_{\vec{k'}\vec{k}} = \frac{2\pi}{\hbar}|\langle\vec{k'}|H_{scatt}|\vec{k}\rangle|^2\rho_{k'} \tag{9}$$

where H_{scatt} is the Hamiltonian for the scattered precesses which conserve both energy and wave vector and $\rho_{k'}$ is the density of final states. For the two scattering mechanisms $P_{\vec{k'}\vec{k}}$ can be expressed as:

$$P^{ac}_{\vec{k'}\vec{k}} = \frac{2\pi}{\hbar}|V^{ac}_{\vec{k'}\vec{k}}|^2\delta(E_{k'} - E_k) \tag{10}$$

$$P^{op}_{\vec{k'}\vec{k}} = \frac{2\pi}{\hbar}|V^{op}_{\vec{k'}\vec{k}}|^2\delta(E_{k'} - E_k \pm \hbar\omega_q) \tag{11}$$

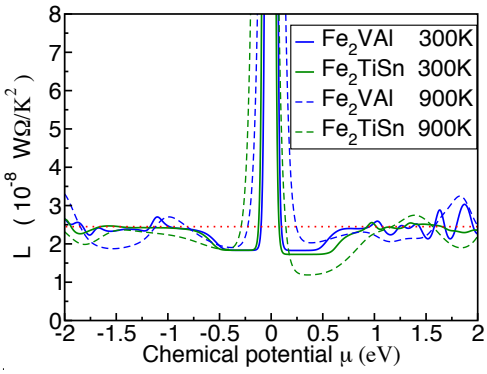

Figure 8: Lorenz function dependence on chemical potential μ of Fe_2VAl and Fe_2TiSn within B1-WC full hybrid using CRYSTAL. The dotted red line shows the Lorenz number L_0.

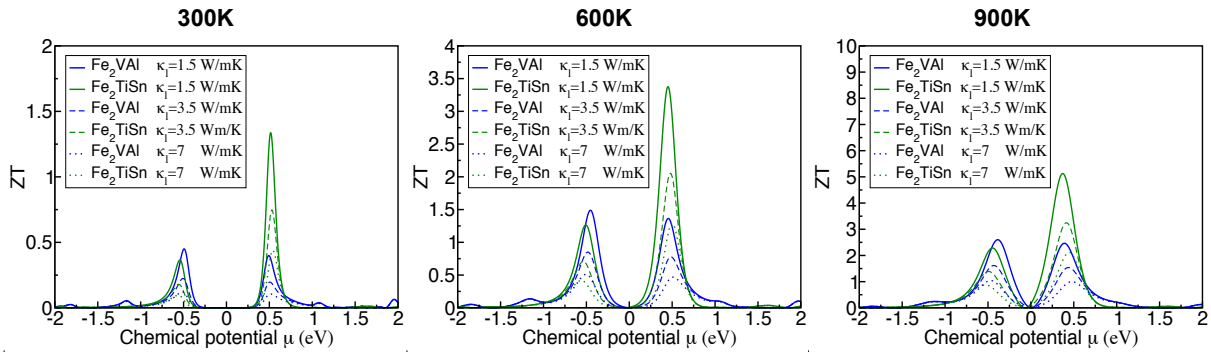

Figure 9: ZT dependence on chemical potential μ and lattice thermal conductivity κ_l for Fe_2VAl and Fe_2TiSn within B1-WC full hybrid and constant relaxation time approximation using CRYSTAL.

where $V^{ac}_{\vec{k'}\vec{k}}$ and $V^{op}_{\vec{k'}\vec{k}}$ are the matrix elements of the acoustic and polar optical interactions, respectively. Considering parabolic $E_k = \hbar^2 k^2/(2m_0)$ energy band dispersion and the property of δ function ($\delta(ax) = [1/a]\delta(x)$), $P^{op}_{\vec{k'}\vec{k}}$ from Eq. 11 can be written as:

$$P^{op}_{\vec{k'}\vec{k}} = \frac{2\pi}{\hbar}|V^{op}_{\vec{k'}\vec{k}}|^2 \frac{m_0}{\hbar^2 kq}\delta(\frac{q}{2k} \mp \cos(\theta) \pm \frac{m_0\omega_{LO}}{\hbar kq}) \tag{12}$$

where θ is the angle between $\vec{k}$ and $\vec{q}$ vectors. At sufficiently high temperature at which the equipartition approximation of the phonon number N_q is valid $N_q \approx N_q + 1 \approx (\kappa_B T)/\hbar\omega_q$, the matrix elements of the interactions are expressed as:

$$|V^{ac}_{\vec{k'}\vec{k}}|^2 = \frac{\hbar E^2_{ac}\omega_q(N_q + 1/2 \pm 1/2)}{\Omega C_l} \approx \frac{E^2_{ac}\kappa_B T}{\Omega C_l} \tag{13}$$

Table 1: The optimized thermoelectric properties of Fe_2TiSn and Fe_2VAl obtained at different values of lattice thermal conductivity and temperature within constant relaxation time approximation. Fe_2VAl values are shown in brackets.

κ_l	n	S	σ	PF	κ_{el}	L	ZT
W/mK	10^{20} cm^{-3}	μV/K	10^3 S/m	10^{-3} W/mK^2	W/mK	10^{-8} WΩ/K^2	
300K							
1.5	2.4	-256	159	10.4	0.83	1.74	1.34
	(0.4)	(-195)	(66)	(2.5)	(0.38)	(1.94)	(0.4)
3.5	3.8	-221	245	11.9	1.28	1.75	0.8
	(0.5)	(-172)	(89)	(2.6)	(0.53)	(1.97)	(0.2)
7	5.1	-198	325	12.8	1.71	1.75	0.44
	(0.6)	(-159)	(107)	(2.7)	(0.64)	(2)	(0.11)
600K							
1.5	3.1	-317	155	15.6	1.27	1.37	3.4
	(0.5)	(-267)	(77)	(5.5)	(0.9)	(1.96)	(1.36)
3.5	4.9	-278	245	18.9	2.02	1.37	2.05
	(0.8)	(-229)	(123)	(6.4)	(1.47)	(1.99)	(0.77)
7	7.3	-246	354	21.4	2.94	1.39	1.29
	(1.1)	(-202)	(173)	(7.1)	(2.1)	(2.03)	(0.47)
900K							
1.5	3.5	-350	140	17.06	1.5	1.19	5.13
	(0.6)	(-321)	(77)	(8)	(1.41)	(2.03)	(2.46)
3.5	5.9	-305	233	21.7	2.51	1.2	3.25
	(1)	(-278)	(131)	(10.1)	(2.41)	(2.04)	(1.54)
7	8.6	-272	339	25.1	3.68	1.21	2.12
	(1.6)	(-245)	(197)	(11.8)	(3.65)	(2.06)	(1)

$$|V^{op}_{\vec{k'}\vec{k}}|^2 = \frac{\hbar e^2(N_q + 1/2 \pm 1/2)}{2\Omega\gamma\omega_{LO}}\frac{1}{q^2}\delta(\vec{k'} - \vec{k} \mp \vec{q}) \approx \frac{e^2\kappa_B T}{2\Omega\gamma\omega^2_{LO}}\frac{1}{q^2}\delta(\vec{k'} - \vec{k} \mp \vec{q}) \tag{14}$$

where E_{ac} is acoustic deformation potential constant, κ_B is Boltzmann constant, C_l is longitudinal elastic constant, $1/\gamma = \omega^2_{LO}(1/\epsilon_\infty - 1/\epsilon_0)$, ϵ_∞ and ϵ_0 are the high frequency and static dielectric permittivities, respectively.

Changing the sums over final $\vec{k'}$ vectors into integrals and using the expressions of matrix elements from Eqs. 13 and 14 , the energy E_k and T dependences of the relaxation times become:

$$\frac{1}{\tau_{ac}(T, E_k)} = \frac{2\pi}{\hbar}\frac{E^2_{ac}\kappa_B T}{\Omega C_l}\frac{\Omega}{(2\pi)^3}4\pi\int_0^\infty dk' k'^2\delta(E_{k'} - E_k) \tag{15}$$

$$\frac{1}{\tau_{ac}(T, E_k)} = \frac{E^2_{ac}\kappa_B T}{\pi\hbar C_l}\frac{2^{1/2}m_0^{3/2}}{\hbar^3}\int_0^\infty dE_{k'}E^{1/2}_{k'}\delta(E_{k'} - E_k) = \frac{2^{1/2}m_0^{3/2}E^2_{ac}\kappa_B}{\pi\hbar^4 C_l}TE_k^{1/2} \tag{16}$$

$$\frac{1}{\tau_{op}(T,E_k)} = \frac{2\pi m_0}{\hbar^3 k}\frac{e^2\kappa_B T}{2\Omega\gamma\omega_{LO}^2}\frac{\Omega}{(2\pi)^3}2\pi\left(\int_{q_{min}^{ab}}^{q_{max}^{ab}}\frac{dq}{q}+\int_{q_{min}^{em}}^{q_{max}^{em}}\frac{dq}{q}\right) \tag{17}$$

$$\frac{1}{\tau_{op}(T,E_k)} = \frac{(2m_0)^{1/2}e^2\kappa_B}{8\pi\hbar^2\gamma\omega_{LO}^2}\left(\ln\left|\frac{\sqrt{1+\hbar\omega_{LO}/E_k}+1}{\sqrt{1+\hbar\omega_{LO}/E_k}-1}\right|+\ln\left|\frac{\sqrt{1-\hbar\omega_{LO}/E_k}+1}{\sqrt{1-\hbar\omega_{LO}/E_k}-1}\right|\right)TE_k^{-1/2} \tag{18}$$

where the limits of q in the integration are determined by setting the argument of δ function from Eq. 12 to zero and solving this equation. For absorption of phonons $q_{min}^{ab} = k(\sqrt{1+\hbar\omega_{LO}/E_k}-1)$, and $q_{max}^{ab} = k(\sqrt{1+\hbar\omega_{LO}/E_k}+1)$, which are obtained for $\theta = 0$ and $\theta = \pi$ respectively. For emission of phonons $q_{min}^{em} = k(1-\sqrt{1-\hbar\omega_{LO}/E_k})$, and $q_{max}^{em} = k(1+\sqrt{1-\hbar\omega_{LO}/E_k})$, which are obtained for $\theta = 0$.

The first order dependence on T and E_k of the acoustic and polar optical relaxation times can be easily identified from the Eqs. 16 and 18 , and this dependence was previously used in literature [26, 27]:

$$\tau_{ac}(T,E_k) = \frac{c_{ac}}{T}E_k^s \tag{19}$$

$$\tau_{op}(T,E_k) = \frac{c_{op}}{T}E_k^s \tag{20}$$

where c_{ac} and c_{op} are constants depending on the scattering mechanism (see Eqs. 16 and 18), E_k is the energy with respect to the bottom of conduction band, and the power exponent s of energies is s=-1/2, and 1/2 for acoustic and polar optical phonon relaxation time, respectively. By fitting the relaxation time for a specific scattering mechanism at a reference temperature T_{ref} (300 K), we express its T dependence for $T > 300$ K, without the use of constants c_{ac} and c_{op}. First, we express E_k dependence of relaxation times in reduced energy $E_k/(\kappa_B T)$:

$$\tau_{ac}(T,E_k) = \frac{c_{ac}}{T}(\kappa_B T)^s\left(\frac{E_k}{\kappa_B T}\right)^s = \tau_{ac}(T)\left(\frac{E_k}{\kappa_B T}\right)^s \tag{21}$$

$$\tau_{op}(T,E_k) = \frac{c_{op}}{T}(\kappa_B T)^s\left(\frac{E_k}{\kappa_B T}\right)^s = \tau_{op}(T)\left(\frac{E_k}{\kappa_B T}\right)^s \tag{22}$$

in order to have proper units of second for the temperature dependent $\tau_{ac}(T)$ and $\tau_{op}(T)$ relaxation times. We have then used $\tau(T,E_k)$ from Eqs. 21 and 22 in the expression of electrical conductivity, which was fitted to experiment at T_{ref}=300K. From this fitting the T dependent terms can be estimated at T_{ref}:

$$\tau_{ac}(T_{ref}) = \tau_{ac}^{ref} = \frac{c_{ac}}{T_{ref}}(\kappa_B T_{ref})^s \tag{23}$$

$$\tau_{op}(T_{ref}) = \tau_{op}^{ref} = \frac{c_{op}}{T_{ref}}(\kappa_B T_{ref})^s \tag{24}$$

from which the constant c_{ac} and c_{op} can be introduced in Eqs. 21 and 22 and the final expressions of $\tau(T, E_k)$, which we use for $T \geq 300$ K are:

$$\tau_{ac}(T, E_k) = \tau_{ac}^{ref} \frac{T_{ref}}{T} \left(\frac{E_k}{\kappa_B T_{ref}} \right)^{-\frac{1}{2}} \tag{25}$$

$$\tau_{op}(T, E_k) = \tau_{op}^{ref} \frac{T_{ref}}{T} \left(\frac{E_k}{\kappa_B T_{ref}} \right)^{\frac{1}{2}} \tag{26}$$

where the reference relaxation time at 300K is τ_{ac}^{ref}=4.3 x 10^{-14} s and τ_{op}^{ref}=2.5 x 10^{-14} s for acoustic and polar optical phonon scattering mechanisms, respectively. The energy E_k dependence is considered relative to the conduction band minimum (carrier pocket minimum energy) and for positive E_k. For $E_k < 0$, only T dependence of $\tau(T)$ is considered ($\tau_{ac}(T)$ = $\tau_{ac}^{ref}(T_{ref}/T)$, and $\tau_{op}(T)$ = $\tau_{op}^{ref}(T_{ref}/T)$).

In Fig. 10 we show the estimated ZT's of Fe_2VAl and Fe_2TiSn considering the acoustic and polar optical phonon relaxation times for a k_l value of 3.5 W/mK. The ZT's are much strongly affected by acoustic phonon scattering, but still large values between 0.6-1.7 can be achieved for the two scattering mechanisms in Fe_2TiSn within the 300-600K intermediate temperature range. These ZT values are significantly larger than those predicted for Fe_2VAl in agreement with experimental data (ZT value of 0.2 estimated at 400K, κ_l=3.3 W/mK, and acoustic scattering in agreement with experiment in $Fe_2V_{0.9}W_{0.1}Al$ alloys (ZT$\sim$0.2) [24]).

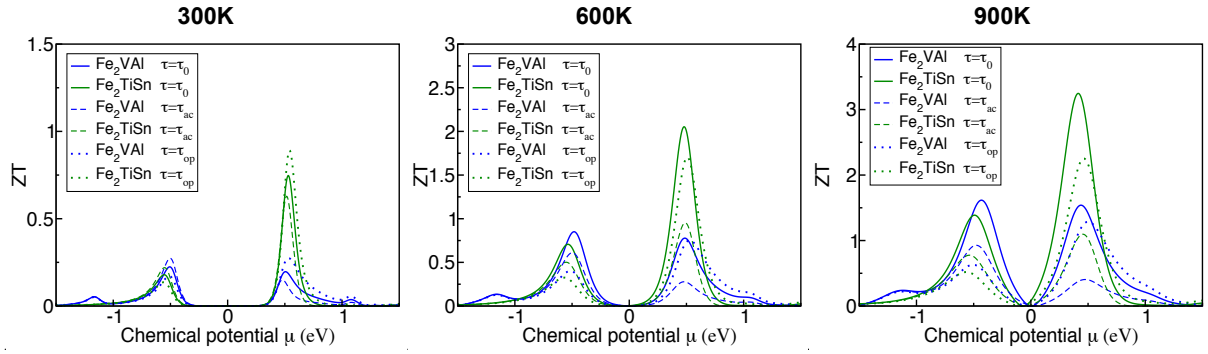

Figure 10: ZT dependence on chemical potential μ and relaxation time τ of Fe_2VAl and Fe_2TiSn estimated for a k_l value of 3.5 W/mK within B1-WC full hybrid using CRYSTAL. The different approximations of τ are: constant relaxation time τ_0, acoustic phonon relaxation time τ_{ac}, and polar optical phonon relaxation time τ_{op}.

1.6 Tendency to the formation of anti-site defects

One important point to mention is that the disorder in X_2YZ full Heusler compounds is relatively high, since their structure is made of four interpenetrating fcc latices. For these compounds

and particularly for X_2YZ semiconductors used in TE applications, site disorder and anti-site defects can significantly affect the electronic properties and should not be neglected. Regarding the TE performance, we showed for Fe_2VAl that site disorder and anti-site defects introduce ingap and resonant d states near the bottom of conduction and top of valence bands which have a detrimental effect on TE properties. [13] We also showed that site disorder can explain the semi-metal character of Fe_2VAl. For this reason we studied the energy stability of X_2YZ regular Heusler *vs* (XY)XZ inverse Heusler structures. We estimated the total energy difference $\Delta E = E_{X2YZ} - E_{(XY)XZ}$ between these structures (see Table 2). Large negative ΔE values implies that X_2YZ regular structure is more stable and (XY) disorder is small, while small negative ΔE values implies the presence of a very large degree of (XY) disorder in X_2YZ regular structure. Our results show that the second set (S2) of Fe_2YZ compounds with Y=Ti, Zr, Hf, and Y=Si, Ge, Sn have less disorder than S1 set with Y=V, Nb, Ta and Y=Al, Ga, In.

Table 2: Total energy difference ΔE between X_2YZ regular and (XY)XZ inverse Heusler structures.

	Fe_2VAl	Fe_2NbAl	Fe_2TaAl	Fe_2TiSi	Fe_2ZrSi	Fe_2HfSi
ΔE(eV)	-1.185	-1.125	-1.208	-1.762	-1.967	-1.662
	Fe_2VGa	Fe_2NbGa	Fe_2TaGa	Fe_2TiGe	Fe_2ZrGe	Fe_2HfGe
ΔE(eV)	-0.807	-0.733	-0.882	-1.362	-2.043	-1.598
	Fe_2VIn	Fe_2NbIn	Fe_2TaIn	Fe_2TiSn	Fe_2ZrSn	Fe_2HfSn
ΔE(eV)	-0.082	-0.664	-1.036	-1.235	-2.219	-1.583

2 Thermodynamical stability

2.1 Technical details

The stability at 0K was assessed using computations in the generalized gradient approximation (GGA) from Perdew Burke and Ernzheroff (PBE) within a plane augmented wave (PAW) approach and using VASP.[28, 29] The computations parameters and pseudopotentials are the ones used in the Materials Project.[31, 32] For each chemical system (e.g., Fe-Ti-Sn), we computed the chemistry in the Heusler crystal structure but also other ternary crystal structures obtained from Heusler-forming systems. The different non-Heusler ternary crystal structure prototypes used in this study are given in Table 2.1.

2.2 Results

The stability of each Heusler phase was evaluated versus all phases present in the Materials Project and our generated ternary phases using the convex hull construction as implemented in

Table 3: Non-Heusler crystal structures prototypes computed as potential competing phases. The identification number of the phase in the Materials Project and the original identification number from the Inorganic Crystal Structure Database (ICSD) are indicated

Formula	Material Project id	icsd id
Fe_2VAl	mp-5778	57832
FeTiSn	mp-22589	106680
Fe_2ZrSi_2	mp-569247	633666
FeHfGe	mp-22191	23577
Fe_3Zr_2Ge	mp-21040	53483
$HfFe_6Ge_6$	mp-19725	53466
$ZrFe_2Si$	mp-19792	87172
FeTiSi	mp-8648	41157
$HfFe_2Si_2$	mp-504741	20933
$HfFeSi_2$	mp-28378	62614
$ZrFeSi_2$	mp-17435	402238
$TiFeSi_2$	mp-21662	31992

the pymatgen package.[30] The convex hull construction effectively compares the energy of a phase versus all linear combinations of other phases.

The energy above the hull and the inverse energy above the hull are measures of stability. The energy above the hull indicates how far from the convex hull formed by all the stable phases is the compound. The larger the energy above the hull the more unstable the compound is. The inverse energy above the hull is only defined for stable phases and is the energy of formation of the compound of interest from the phases that would be stable if the compound did not exist. The larger the inverse energy above the hull the more stable the compound is. More information on those measures of stability can be found in Refs. [34] and [33]. Table 4 gives numerical values for the stability measure and the decomposition products (if unstable) for all computed Heusler compounds. References to experimental literature referring to the synthesis of those Heusler phases are also indicated. The stability energy is the inverse energy above the hull when stable (negative number) and the energy above the hull when unstable (positive number).

As an example of the method, the phase diagrams for Fe_2VAl and Fe_2TiSn are shown in Figures 11 and 12. All computed compounds in the Fe-V-Al and Fe-Ti-Sn systems are shown in the phase diagrams. The stability energy of each compound is given by the color mapping on the right. It is clear that the Fe_2VAl and Fe_2TiSn are predicted stable with respect to their competing phases. Figure 13 gathers the stability energies for all studied Heusler compounds.

Table 4: Phase stability at 0K for all Heusler phases. The energy indicates the energy above the hull when positive (unstable) and the inverse energy above the hull when negative (stable). The decomposition products indicates to which compounds the unstable Heusler phase will decompose.

Formula	Energy (meV/atom)	Decomposition products	Experimental evidences
Fe_2TaAl	-203.3		[42]
Fe_2VAl	-199.2		[35, 36, 37, 38]
Fe_2VGa	-148.6		[37, 39]
Fe_2NbAl	-135.6		[38]
Fe_2TiSi	-135.5		[40]
Fe_2TiGe	-72.7		None
Fe_2TaGa	-64.3		None
Fe_2TiSn	-52.1		[41, 25]
Fe_2NbGa	-28.6		None
Fe_2HfSn	19.5	$HfFe_2$ + Sn	None
Fe_2HfSi	51.8	Hf_2Fe_3Si + $HfFe_2Si_2$ + Fe_3Si	None
Fe_2ZrSn	59.7	Fe + Sn + Zr_5Sn_4	None
Fe_2HfGe	61.8	HfFeGe + Fe	None
Fe_2ZrSi	112.4	Zr_2Fe_3Si + $ZrFe_4Si_2$ + ZrFeSi	None
Fe_2ZrGe	118.7	ZrFeGe + Fe	None
Fe_2NbIn	130.7	$NbFe_2$ + In	None
Fe_2TaIn	131.7	$TaFe_2$ + In	None
Fe_2VIn	164.0	Fe + VFe + In	None

Figure 11: Phase diagram of Fe_2VAl

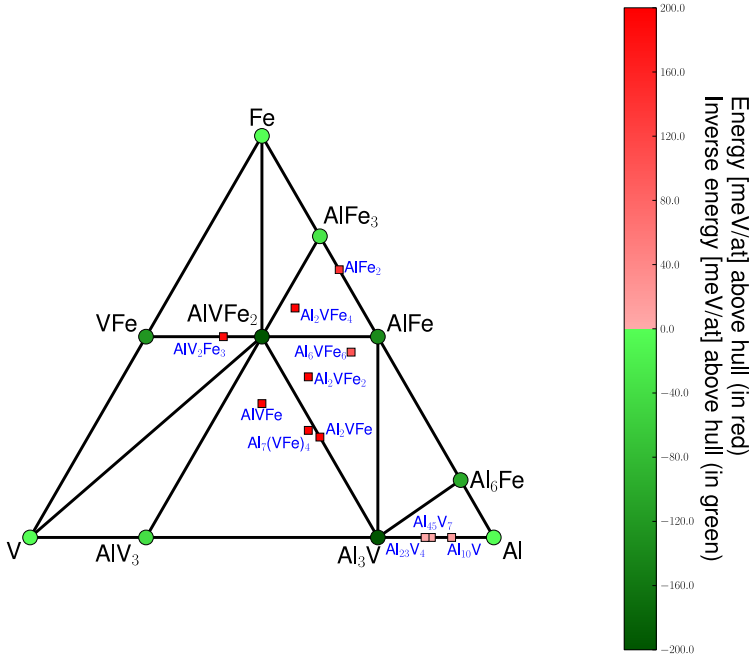

Figure 12: Phase diagram of Fe_2TiSn

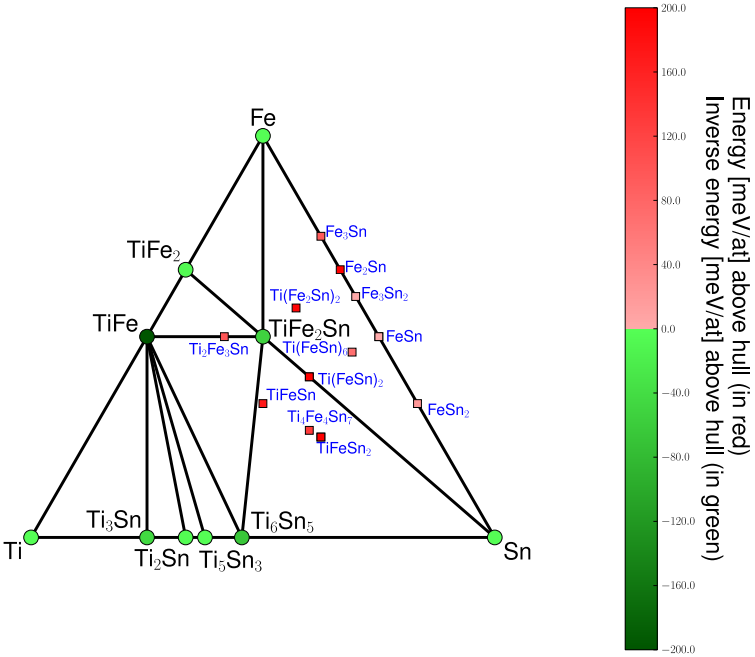

Figure 13: Phase stability at 0K for all Heusler phases. The energy indicates the energy above the hull when positive (unstable) and the inverse energy above the hull when negative (stable). The subfigure a relates to IV-IV Heuslers and subfigure b to III-V Heuslers

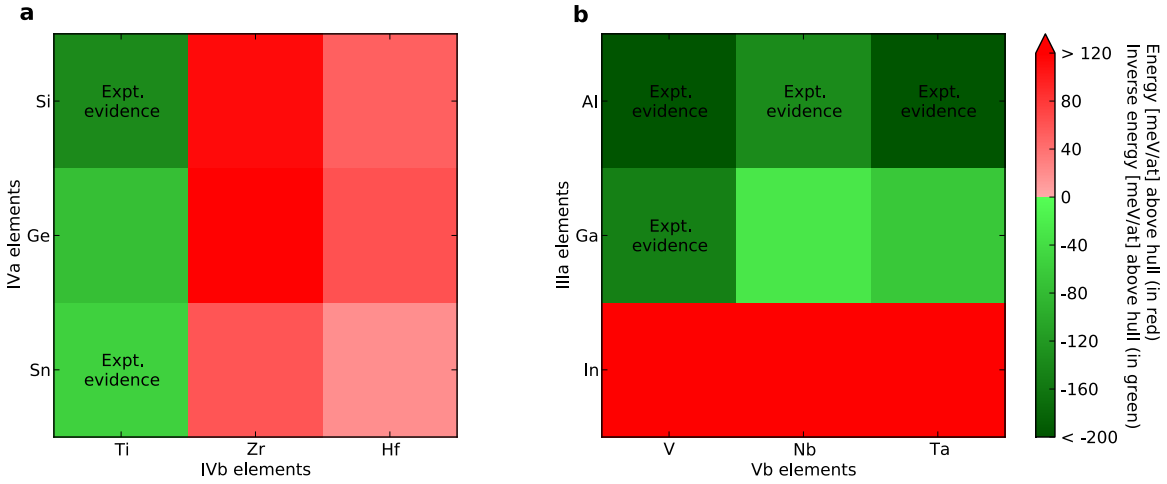

References

[1] R. Dovesi, R. Orlando, B. Civalleri, C. Roetti, V. R. Saunders, and C. M. Zicovich-Wilson, Z. Kristallogr. **220**, 571 (2005).

[2] I. de P. R. Moreira, R. Dovesi, C. Roetti, V. R. Saunders, R. Orlando, Phys. Rev. B **62**, 7816 (2000).

[3] E. Ruiz, M. Llunell, P. Alemany, J. Solid State Chem. **176**, 400 (2003).

[4] http://www.tcm.phy.cam.ac.uk/∼mdt26/crystal.html

[5] http://www.crystal.unito.it/Basis_Sets/Ptable.html

[6] R. Pandey, M. Causa, N. M. Harrison, M. Seel, J. Phys.: Condens. Matter **8**, 3993 (1996).

[7] T. Bredow, P. Heitjans , M. Wilkening, Phys. Rev. B **70**, 115111 (2004).

[8] D. Munoz-Ramo, J. L. Gavartin, A. L. Shluger, Phys. Rev. B **75**, 205336 (2007).

[9] A. R. Porter, M. D. Towler, R. J. Needs, Phys. Rev. B **60**, 13534 (1999).

[10] D. I. Bilc, R. Orlando, R. Shaltaf, G.-M. Rignanese, J. Iniguez, and Ph. Ghosez, Phys. Rev. B **77**, 165107 (2008).

[11] Z. Wu, R. E. Cohen, Phys. Rev. B **73**, 235116 (2006).

[12] A. D. Becke, J. Chem. Phys. **104**, 1040 (1996).

[13] D. I. Bilc, P. Ghosez, Phys. Rev. B **83**, 205204 (2011).

[14] M. Goffinet, P. Hermet, D. I. Bilc, and Ph. Ghosez, Phys. Rev. B **79**, 014403 (2009).

[15] A. Prikockyte, D. Bilc, P. Hermet, C. Dubourdieu, and P. Ghosez, Phys. Rev. B **84**, 214301 (2011).

[16] G. K. H. Madsen, D. J. Singh, Comput. Phys. Commun. **175**, 67 (2006).

[17] Y. Nishino, S. Deguchi, U. Mizutani, Phys. Rev. B **74**, 115115 (2006).

[18] M. Vasundhara, V. Srinivas, V. V. Rao, Phys. Rev. B **77**, 224415 (2008).

[19] Ye Feng *et al.*, Phys. Rev. B **63**, 165109 (2001).

[20] S. V. Dordevic, D. N. Basov, A. Slebarski, M. B. Maple, and L. Degiorgi, Phys. Rev. B **66**, 075122 (2002).

[21] P. Blaha *et al.*, WIEN2K, An Augmented PlaneWave+Local Orbitals Program for Calculating Crystal Properties, Techn. Universitat Wien, Austria, 2001.

[22] D. J. Singh, I. I. Mazin, Phys. Rev. B **57**, 14352 (1998).

[23] D. M. Rowe, V. L. Kuznetsov, L. A. Kuznetsova, G. Min, J. Phys. D : Appl. Phys. **35**, 2183 (2002).

[24] M. Mikami, Y. Kinemuchi, K. Ozaki, Y. Terazawa, and T. Takeuchi, J Appl. Phys. **111**, 093710 (2012).

[25] C. S. Lue, Y.-K. Kuo, J. Appl. Phys. **96**, 2681 (2004).

[26] A. Popescu, L. M. Woods, J. Martin, and G. S. Nolas, Phys. Rev. B **79**, 205302 (2009).

[27] D. I. Bilc, S. D. Mahanti, and M. G. Kanatzidis, Phys. Rev. B **74**, 125202 (2006).

[28] G. Kresse, J. Furthmüller, Comput. Mater. Sci. **6**, 15 (1996).

[29] J. Perdew, K. Burke, M. Ernzerhof, Phys. Rev. Lett. **77**, 3865 (1996).

[30] S. P. Ong *et al.*, Comput. Mater. Sci. **68**, 314 (2013).

[31] A. Jain *et al.*, Comput. Mater. Sci. **50**, 2295 (2011).

[32] Materials Project, http://www.materialsproject.org

[33] H. Chen, G. Hautier, G. Ceder, J. Am. Chem. Soc. **134**, 19619 (2012).

[34] G. Hautier, S. P. Ong, A. Jain, C. J. Moore, G. Ceder, Phys. Rev. B **85**, 155208 (2012).

[35] C. Liu, D. T. Morelli, J. Electron. Mat. **41**, 1632 (2012).

[36] Y. Nishino, IOP Conf. Ser.: Mater. Sci. Eng. **18**, 142001 (2011).

[37] C. S. Lue *et al.*, J. Phys.: Condens. Matter **13**, 1585 (2001).

[38] C. S. Lue, R. F. Liu, M. Y. Song, K. K. Wu, Y. K. Wuo, Phys. Rev. B **78**, 165117 (2008).

[39] A. Ślebarski, J. Goraus, Phys. Rev. B **80**, 235121 (2009).

[40] M. Perrier *et al.*, Metall. Mater. Trans. A **43**, 4999 (2012).

[41] M. Nakabayashi *et al.*, Physica B **329**, 1134 (2003).

[42] http://www.mpie.de/fileadmin/annual_reports/Annual_Report_2011_2012.pdf, p. 92.

Author Contributions D.I.B and Ph.G. designed the project on the electronic and thermoelectric properties. G.H., D.W. and G.-M.R. added the investigation on the thermodynamical stability. D.I.B. performed the computation of the electronic and thermoelectric properties, while D.W. ran the calculations regarding the thermodynamical stability of the different compounds. All authors analyzed and interpreted the data. D.I.B. wrote the article while all authors discussed and edited it.

Author Information The authors declare no competing financial interests. Correspondence should be addressed to D.I.B. (Daniel.Bilc@itim-cj.ro) and Ph.G. (Philippe.Ghosez@ulg.ac.be).